TASK IV: Development of Circumferential Inlet Distortion through a Representative Eleven Stage High-speed Axial Compressor

Summary

The concepts and the procedure developed in Task I and Task III were used to determine the response of an eleven-stage high-speed compressor to an inlet distortion of 180^0 circumferential extent for contrasting against its performance under uniform inlet flow. Using the computed results at the inlet to and outlet of the compressor, the computed total pressure ratio and efficiency for the clean condition are determined to be 14.22 and 76.9% respectively. As for the distorted case, these are determined to be 10.35 and 71.8% respectively, showing deterioration in both the computed total pressure ratio (14.22 vs 10.35) and the efficiency (76.9% vs 71.8%).

The physical consistency of the computed flow field was assessed as a means of demonstrating the applicability and utility of the body force representation for inlet distortion computations. Specifically the computed evolution of the distorted pattern in static pressure and total pressure from compressor inlet to exit is examined.

For the eleven-stage compressor examined here, the deterioration in performance has been found to be particularly severe in the last 2 stages. This suggests that the last two stages could be redesigned to alleviate the observed deterioration thus making the compressor performance insensitive to circumferential inlet distortion. This can potentially be accomplished by first determining what should the body force distribution of the last two stages should be to achieve minimal or no deterioration in performance in the last two stages. One can then in principle proceed to determine the blade design to yield such a body force distribution.

1.0 Introduction

Results from computing the response of an eleven stage high-speed compressor (representative of current design) to a circumferential inlet distortion are described in Task IV here. Section 2.0 briefly described the procedure used and key results are presented in Section 3.

2.0 Technical Approach And Methodology

This section presents the framework for the use of body forces to represent blade row effects. This is followed by a presentation of the implementation of the methodology for computing the axisymmetric flow field and the response of an 11-stage compressor to circumferential inlet distortion.

2.1 Governing Equations

Within a blade row, by integrating the unsteady, three-dimensional, compressible Navier-Stokes equations in the circumferential direction, a system of unsteady axisymmetric equations in the x-r plane is obtained. These equations contain terms representing "body forces". The resulting equations incorporating body forces are given by

$$\frac{\partial(b\overline{U})}{\partial t} + \frac{\partial(b\overline{F}_{inv})}{\partial x} + \frac{\partial(b\overline{H}_{inv})}{\partial r} = b\overline{S} + \overline{F} \qquad (2.1)$$

where the overbar represents a circumferentially averaged property, and

$$
\overline{U} = \begin{vmatrix} r\overline{\rho} \\ r\overline{\rho}\,\overline{V}_x \\ r\overline{\rho}\,\overline{V}_\theta \\ r\overline{\rho}\,\overline{V}_r \\ r\overline{\rho}\,\overline{e}_t \end{vmatrix},\
\overline{F}_{inv} = \begin{vmatrix} r\overline{\rho}\,\overline{V}_x \\ r(\overline{\rho}\,\overline{V}_x^{\,2} + \overline{p}) \\ r\overline{\rho}\,\overline{V}_x\overline{V}_\theta \\ r\overline{\rho}\,\overline{V}_x\overline{V}_r \\ r\overline{V}_x(\overline{\rho}\,\overline{e}_t + \overline{p}) \end{vmatrix},\
\overline{H}_{inv} = \begin{vmatrix} r\overline{\rho}\,\overline{V}_r \\ r\overline{\rho}\,\overline{V}_x\overline{V}_r \\ r\overline{\rho}\,\overline{V}_\theta\overline{V}_r \\ r(\overline{\rho}\,\overline{V}_r^{\,2} + \overline{p}) \\ r\overline{V}_r(\overline{\rho}\,\overline{e}_t + \overline{p}) \end{vmatrix},\
\overline{S} = \begin{vmatrix} 0 \\ 0 \\ -\overline{\rho}\,\overline{V}_\theta\overline{V}_r \\ \overline{\rho}\,\overline{V}_\theta^{\,2} + \overline{p} \\ 0 \end{vmatrix},\
\overline{F} = \begin{vmatrix} 0 \\ r\overline{\rho}f_x \\ r\overline{\rho}f_\theta \\ r\overline{\rho}f_r \\ r\overline{\rho}(\vec{f}\cdot\vec{V}) \end{vmatrix}
$$

$\vec{f}$ is the body force per unit mass with components f_x, f_θ and f_r; and b is a blockage factor defined as the ratio of the angular pitch at a general point (x,r) to that at the leading edge. Its value corresponds to 1 for blades with zero thickness and to some value less than 1 when blades of finite thickness are present.

431

Eq. (2.1) shows that the action of a blade-row on the flow may be represented by an axisymmetric flow field in pitchwise-averaged flow properties and an appropriately derived distributed body force $\vec{f}(x,r)$. Physically, this is equivalent to using an infinite number of blades, with the flow being axisymmetric in each infinitesimal blade passage. As described in Task 1 to Task 3, such a representation is adequate for assessing the response of a blade row or compressor to circumferential flow non-uniformity with length scale larger than a blade pitch.

In the work described in this Task, Eq. (2.1) is solved numerically using the CFD code used for Task 1 and Task 3. The equations are discretized spatially and, using zero flow and zero compressor speed conditions as the initial condition, are marched in time using the five-step Runge-Kutta time-marching scheme. The imposed boundary conditions are total pressure, total temperature and flow angles at the upstream boundary, as well as throttle setting.

2.2 Description of the 11-stage Axial Compressor

The 11-stage axial compressor, representative of current design, comprises an IGV followed by 11 stages, leading to 23 blade rows in total. The configuration is shown in Fig. 2.1. The procedure for implementation of the body force representation is presented in Sections 2.3. A representative grid with a resolution of 342x80x12 is shown in Fig. 2.2.
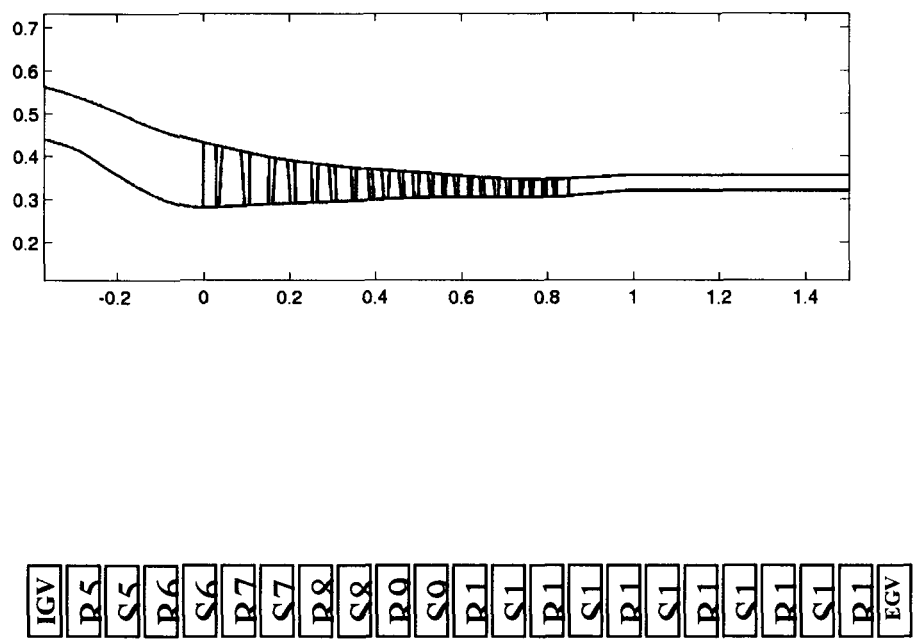
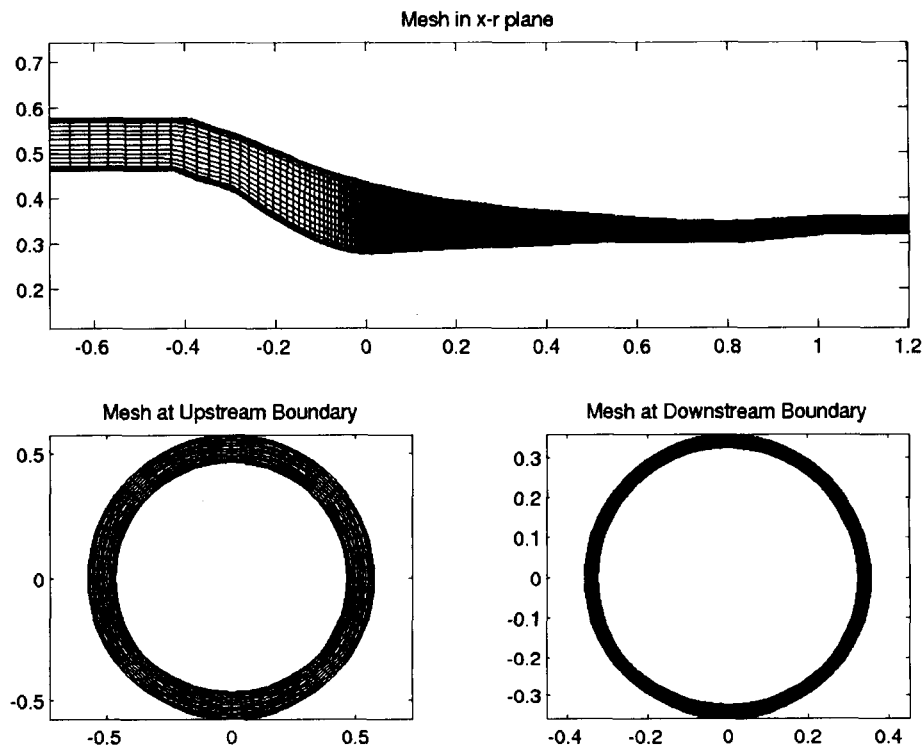Fig. 2.1 Configuration of 11-stage Axial Compressor

Fig. 2.2 Mesh for the 11-stage Compressor (342x80x12)

2.3 Implementation of Methodology for Computing Compressor Response to Inlet Distortion

For the case of inlet distortion, a total pressure distortion is imposed at the upstream boundary. The low and high total pressure regions each occupy a circumferential extent of 180^0 and the distortion is defined by $\dfrac{P_{t,high} - P_{t,low}}{\dfrac{1}{2}\rho U^2} = 0.49$. The flow field and total pressure ratios are computed at a corrected mass flow of 53.94 kg/s. To determine the effects of inlet distortion on the performance of the compressor, the total pressure ratio for an axisymmetric flow at the same corrected mass flow is computed. For both axisymmetric flow and inlet distortion, the transient phase of the computations requires the body forces to vary transiently in response to a time-varying flow field.

The local blade force comprises of 2 components, $\vec{F}_n$ which is normal to the blade and $\vec{F}_p$ which is parallel to the blade. $\vec{F}_n$ is considered to be due to the pressure loading and $\vec{F}_p$ the viscous shear. It can be shown that these force components depend on local flow properties. The relationship can be expressed as

$$\vec{F}_n = -K_n(\Delta\beta, M, \text{Re})\frac{(\vec{V}_{rel} \cdot \hat{\eta})(\vec{V}_{rel} \cdot \hat{\xi})}{h}\hat{n} \tag{2.2}$$

$$\vec{F}_p = -K_p(\Delta\beta, M, \text{Re})\frac{\vec{V}_{rel} \cdot \vec{V}_{rel}}{h}\hat{p} \tag{2.3}$$

K_n and K_p are coefficients, which, in general, depend on local deviation angle $\Delta\beta$, Mach number M and Reynolds number Re. $\vec{V}_{rel}$ is the relative velocity vector. $\hat{\eta}$ and $\hat{\xi}$ are unit vectors parallel and normal to the blade surface respectively. $\hat{n}$ and $\hat{p}$ are unit vectors normal and parallel to $\vec{V}_{rel}$ respectively.

In this work, K_n and K_p are assumed constant and are determined from

$$K_n = 4.2 - 2\alpha \tag{2.4}$$

$$K_p = 0.04 \tag{2.5}$$

The use of Eqns. (2.4) and (2.5) is motivated by their simplicity and ability to reproduce loss and deviation trends in cascades. The results and discussion of the compressor response to inlet distortion based on the formulation described by Eqns. (2.2) to (2.5) are presented in Section 3.

435

3.0 Results And Discussion For Inlet Distortion Computations

In this section, results for the calculation of the 11-stage compressor under circumferential inlet distortion are presented. The procedure has been presented in Section 2.0. The flow field is analyzed for self consistency as a means for assessing the applicability of the body force representation to determine multi-stage high-speed axial compressor response to inlet distortion and to determine which specific stage is less tolerant to circumferential distorted flow.

The analysis begins with the observation of deterioration, as compared to axisymmetric flow, in overall total pressure ratio and efficiency under distorted inlet flow (Section 3.1.1). Closer examination of the total pressure ratio and efficiency of the individual stages shows that this deterioration is due largely to the last 2 stages (Section 3.1.2). The particularly severe deterioration in total pressure ratio in these stages is associated with the manner in which the distortion travels from the far upstream boundary to the IGV inlet (Section 3.3) and then through the 11 stages (Section 3.4). These points will be elaborated upon in the following sections.

3.1 Compressor Performance

3.1.1 Overall Performance

For the same corrected mass flow, the total pressure ratio and adiabatic efficiency of the whole compressor for each inlet condition is tabulated in Table 3.1.

Inlet Condition	Corrected Mass Flow (kg/s)	Total Pressure Ratio	Adiabatic Efficiency (%)
Axisymmetric	53.94	14.22	76.9
Distorted	53.94	10.35	71.8

Table 3.1 Compressor Performance for Axisymmetric and Distorted Inlet Flow

The compressor experiences deterioration in total pressure ratio and efficiency as a result of inlet distortion. It will be shown in subsequent sections that the deterioration is

associated with the behavior of a static pressure distortion which is eliminated over the last 2 stages.

The efficiency data in Table 3.1 is computed using total pressure and total temperature ratios. To assess the consistency of the computed efficiencies, these are calculated by using another approach that involves the losses generated by the body force representation and the increase in entropy across gaps between blade rows.

As loss can be quantified by increase in entropy, it is useful to relate the efficiency of a compressor to the increase in entropy according to the following equation

$$\eta = \frac{\pi^{\gamma-1/\gamma} - 1}{\left(\pi e^{\Delta s/R}\right)^{\gamma-1/\gamma} - 1} \tag{3.1}$$

where π is the total pressure ratio of the compressor.

In the body force representation, losses are generated in blade rows through the dissipative work term $\vec{F}_p \cdot \vec{V}_{rel}$, where $\vec{F}_p$ is the force component in the direction of the relative velocity $\vec{V}_{rel}$. This can be used to calculate the entropy increase due to the 23 blade rows. The rate of entropy generation for each blade row is calculated by a summation over the finite volume cells and is given by

$$\dot{S}_b = \sum_{cells} \frac{\vec{F}_p \cdot \vec{V}_{rel}}{T} \tag{3.2}$$

The change in entropy per unit mass across the blade row, Δs_b, is determined from the difference in entropy flux across the blade row.

$$\Delta s_b = \frac{\dot{S}_b}{\dot{m}} \tag{3.3}$$

The total change in entropy of the 23 blade rows is given by

$$\Delta s_{bt} = \sum_{\substack{blade \\ rows}} \Delta s_b \tag{3.4}$$

437

For gaps between blade rows, the entropy increase across each gap is determined from

$$\Delta s_g = c_p \ln \tau_g - R \ln \pi_g \qquad (3.5)$$

where τ_g and π_g are static temperature and static pressure ratios across the gap respectively. The total change in entropy of the 22 gaps is given by

$$\Delta s_{gt} = \sum_{gaps} \Delta s_g \qquad (3.6)$$

To separate the effects of blade rows and gaps on efficiency, the efficiency is first calculated from Eq. (3.1) using $\Delta s = \Delta s_{bt}$ (blade rows only) and then using $\Delta s = \Delta s_{bt} + \Delta s_{gt}$ (blade rows and gaps). The results for each inlet condition are tabulated in Table 3.2.

Inlet Condition	η (Blade Rows Only)	η (Blade Rows and Gaps)	Δη Due to Gaps
Clean	78.2%	76.6%	1.6%
Distorted	73.7%	71.4%	2.3%

Table 3.2 Adiabatic Efficiency Calculated from Losses in Blade Rows and Gaps

The data of Table 3.2 demonstrates that the effects of gaps can be significant in a compressor with a large number of gaps (22 in the case of the 11-stage compressor) in which numerical dissipations occur. The larger decrement in calculated efficiency of 2.3% for distorted flow (as shown in the far right column of Table 3.2) as compared to 1.6% for clean flow could be due to numerical dissipation in the circumferential direction. The contribution from numerical dissipation in principle can be quantified through implementation of additional calculations with varying degrees of grid resolution and through extrapolation of the computed results. However, this has not been done here.

The computed distribution of entropy rise across the stages for clean and distorted inlet flow conditions is shown in Figs. 3.1(a) and (b) respectively. Entropy rise is defined non-dimensionally as $\dfrac{T_{ref}\Delta s}{U_{ref}^2}$. It is observed that for rotors, losses are highest for the first and

last stages. For stators, losses are highest for the first stage. The entropy rise across gaps is highest at the last stage.

3.1.2 Stage Performance

For distorted flow, the deterioration in total pressure ratio over the clean flow condition is calculated in each of the 11 stages and presented in Fig. 3.2. This deterioration is defined by the ratio $\dfrac{\pi_{clean} - \pi_{distorted}}{\pi_{ave} - 1}$, where π_{clean} and $\pi_{distorted}$ are stage total pressure ratios for the clean and distorted inlet conditions respectively. π_{ave} is the average stage total pressure ratio for the 11 stages. The deterioration can be seen to be particularly severe in the last 2 stages.

The percentage decrease in efficiency, defined as $\left(\dfrac{\eta_{clean} - \eta_{distorted}}{\eta_{clean}} \right) \times 100\%$, for each stage is shown in Fig. 3.3. The deterioration in efficiency is found to be most severe in the last 2 stages.
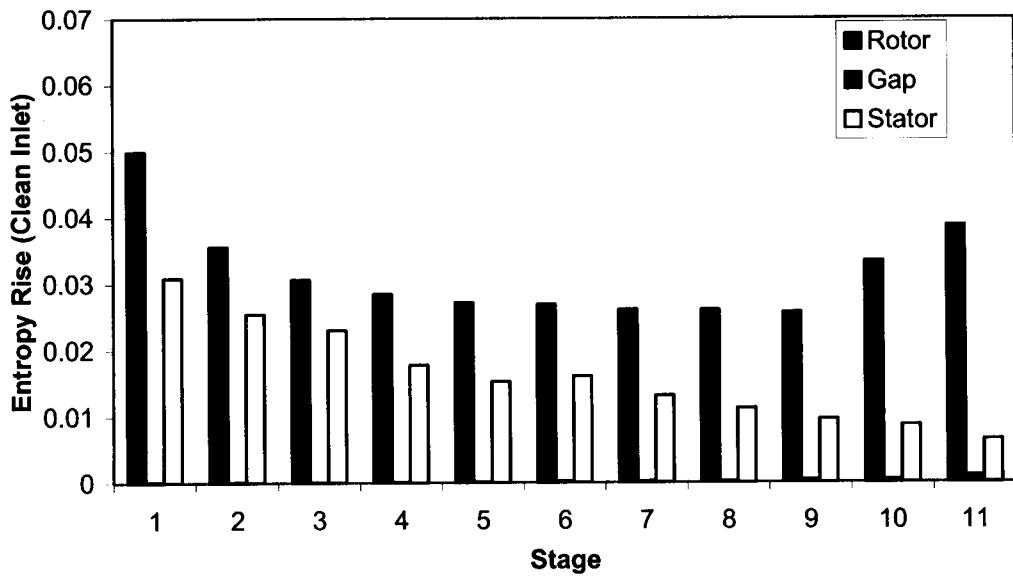
(a)
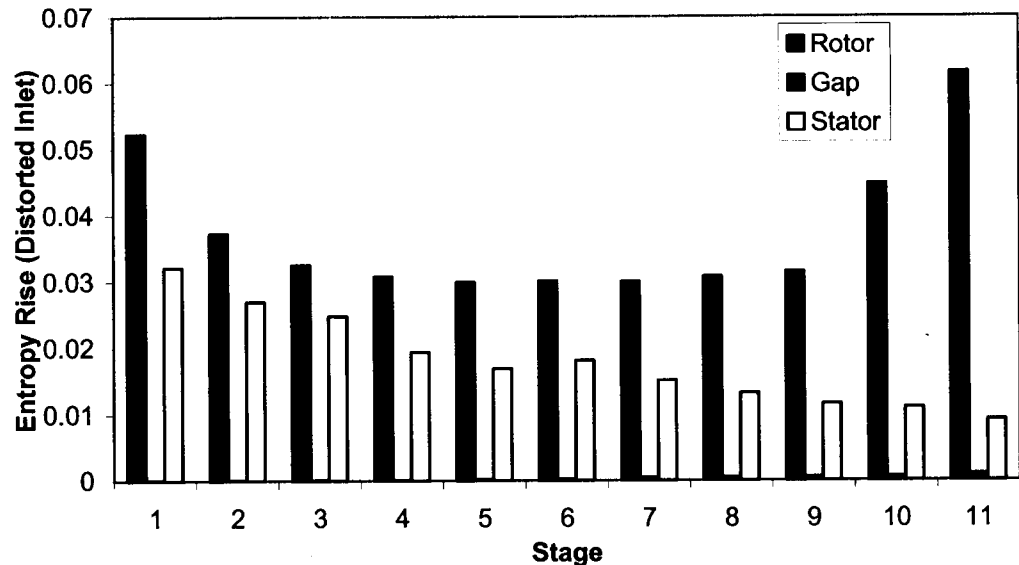
(b)

Fig. 3.1 Distribution of Entropy Rise Across the Stages for (a) Clean Inlet Flow
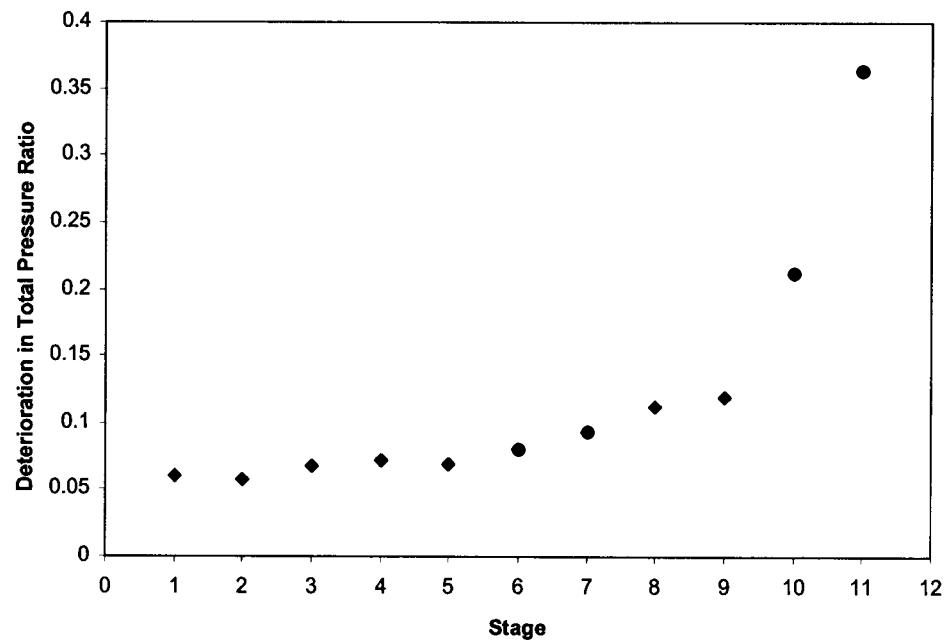
(b) Distorted Inlet Flow

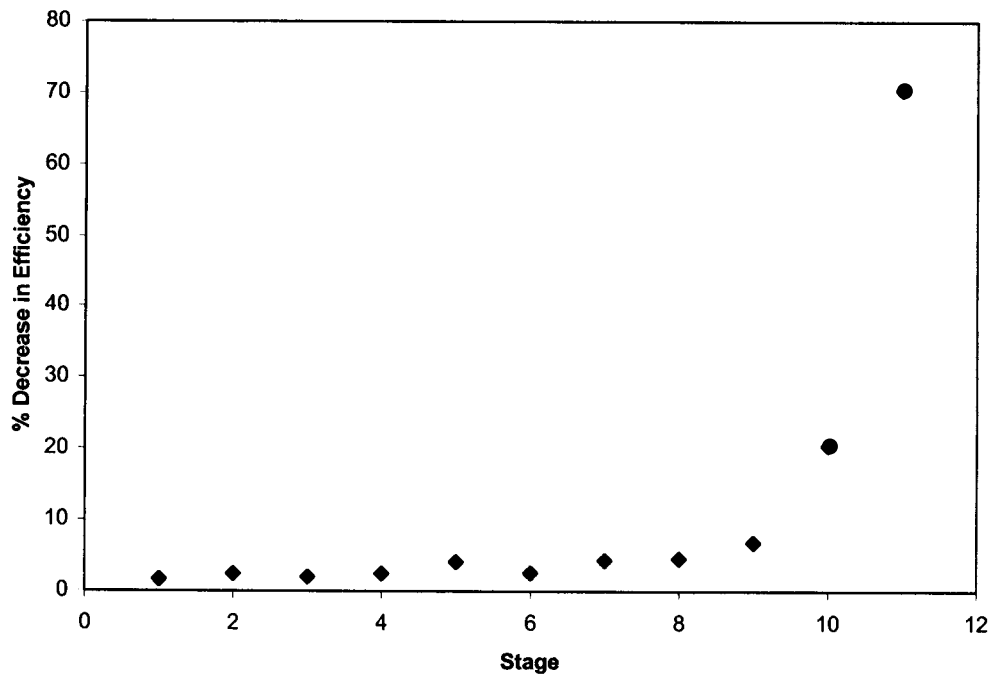Fig. 3.2 Deterioration in Stage Total Pressure Ratio

Fig. 3.3 Deterioration in Efficiency

It can be seen from the data of Figs. 3.2 and 3.3 that, although the same computational model (Eqns. (2.2) to (2.5)) is used in all the stages to compute the body forces from local flow conditions, inlet distortion produces varying degrees of performance deterioration among the stages. Certain stages are found to be insensitive to inlet distortion as compared to other stages (for example, from Figs. 3.2 and 3.3, the first 3 stages are insensitive to inlet distortion as compared to the last 2 stages). This suggests, hypothetically, that it may be possible to design a compressor that is insensitive to inlet distortion by modifying Eqns. (2.2) to (2.5) appropriately. The resulting body force representation can then be used to determine the blade geometry of a compressor whose performance does not deteriorate significantly with inlet distortion.

The particularly severe deterioration in performance in the last two stages is associated with the formation of a static pressure distortion at the IGV inlet (Section 3.3), its amplification through the first 9 stages (Section 3.4.1) and its abrupt elimination through the final 2 stages (Section 3.4.2). These will be described in the following sections as part of an analysis of the computed flow field. The physical consistency of the computed flow field will also be assessed as a means of demonstrating the utility of the body force representation for inlet distortion computations.

3.2 Static Pressure at Compressor Outlet

The static pressure at the compressor outlet appears to have an important effect on the manner in which the inlet distortion propagates from the upstream boundary and through the compressor.

The computed mid-radius static pressure (defined as P/P_{ref} where P_{ref} is reference pressure, selected to be the total pressure at the upstream boundary. Plots of static pressure will use this definition hereon) at the compressor exit is shown in Fig. 3.4 and is examined for consistency with the condition of circumferential uniformity before beginning an analysis of the propagation of the distortion. This can be seen to be uniform circumferentially as expected.
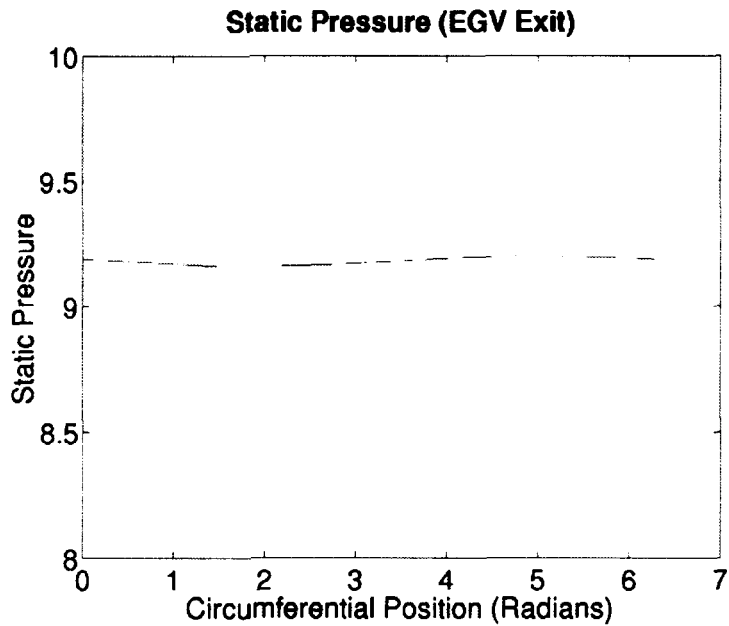
Static Pressure (EGV Exit)

Fig. 3.4 Computed Mid-radius Static Pressure at Compressor Exit

3.3 Distortion Behavior from Upstream Boundary to IGV Inlet

Two essential phenomena will be analyzed for consistency in this section. The first phenomenon is the formation of a static pressure distortion at the IGV inlet. This gives rise to changes in the velocity distortion and the circumferential extent of the low total pressure section of the distortion, as well as an induced swirl. The second one is the asymmetric character of the velocity distortion at the IGV inlet.

3.3.2 Formation of Static Pressure Distortion at IGV Inlet

The change in circumferential extent of the low total pressure section can be explained by first considering the result presented previously in Section 3.1, that static pressure is uniform at the compressor exit. Also, in compressors, the variation of static pressure rise ψ

(defined as $\dfrac{\Delta P_s}{\frac{1}{2}\rho U^2}$) with flow coefficient ϕ follows a decreasing trend as shown in Fig. 3.5.
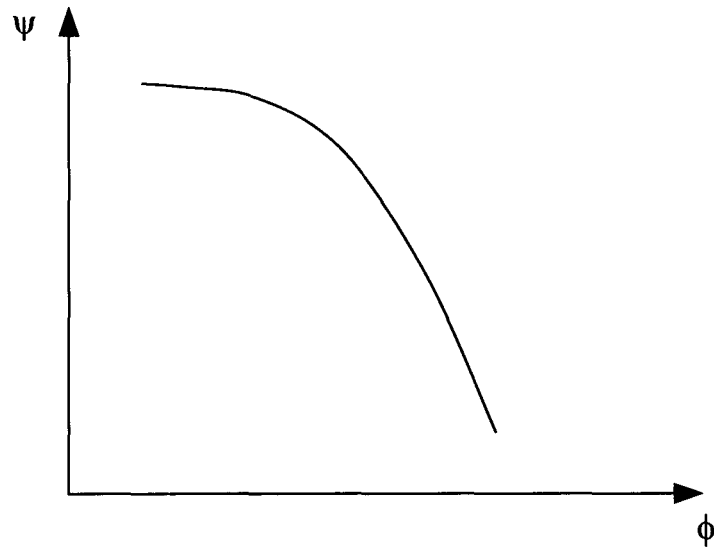
443

Fig. 3.5 Variation of Pressure Rise with Flow Coefficient

The region of lower flow in the distorted sector corresponds to higher loading, and hence static pressure there is reduced as the inlet distortion travels from the upstream boundary (where static pressure is circumferentially uniform) to the IGV inlet, leading to a static pressure distortion at the IGV inlet. The reduction in static pressure also leads to an increase in velocity (conversely, the static pressure and velocity in the high total pressure region are increased and decreased respectively), leading to an attenuation of the velocity distortion at the IGV inlet. By continuity and knowing that total pressure is convected with streamlines, the circumferential extent of the low total pressure region is expected to be reduced as it travels towards the IGV inlet, giving rise to an induced swirl.

The computed flow field is examined for consistency with the expected flow features. The computed mid-span static pressure at the IGV inlet as shown in Fig. 3.6 indicates that a static pressure distortion does indeed form at the IGV inlet. The computations also reveal the associated attenuation in the velocity distortion as shown in Fig. 3.7 which are plots of the mid-span flow coefficient at the upstream boundary (Fig. 3.7(a)) and IGV inlet (Fig.3.7(b)). The computed mid-span total pressures (defined as P_t/P_{ref} where P_{ref} is reference pressure, selected to be the total pressure at the upstream boundary) at the upstream boundary and the IGV inlet show consistency with the expected reduction in

444

circumferential extent of the low total pressure region, as indicated in Fig. 3.8. Finally, the existence of an induced swirl can be seen from the plot of mid-span flow angles at the IGV inlet, as shown in Fig. 3.9.
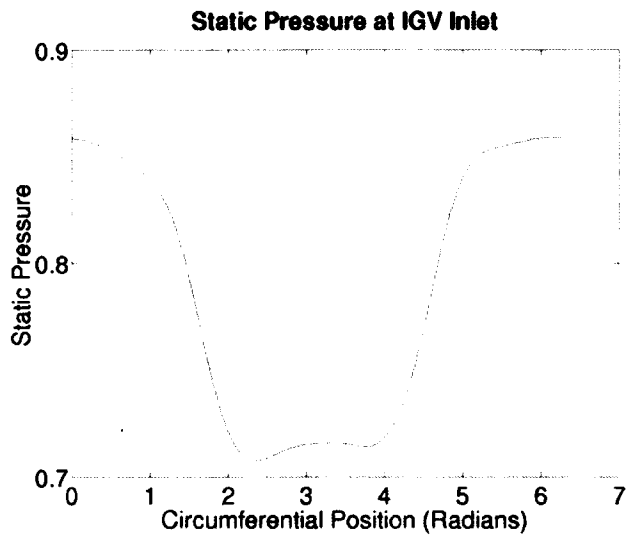
Static Pressure at IGV Inlet

Fig. 3.6 Static Pressure Distortion at the Mid-span of the IGV Inlet

(a)   (b)
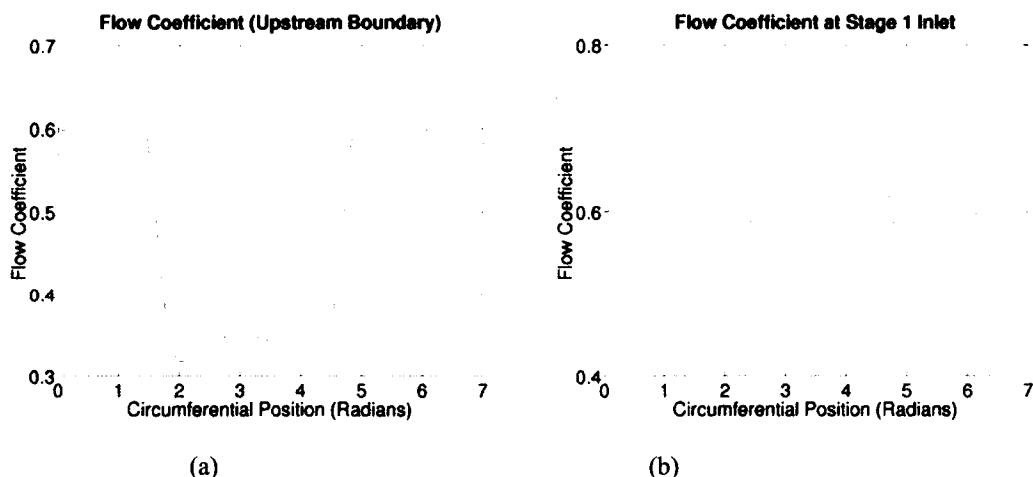
Fig. 3.7 Mid-span Velocity Distributions at (a) Upstream Boundary and (b) IGV Inlet, Showing Attenuation of the Velocity Distortion at the IGV Inlet
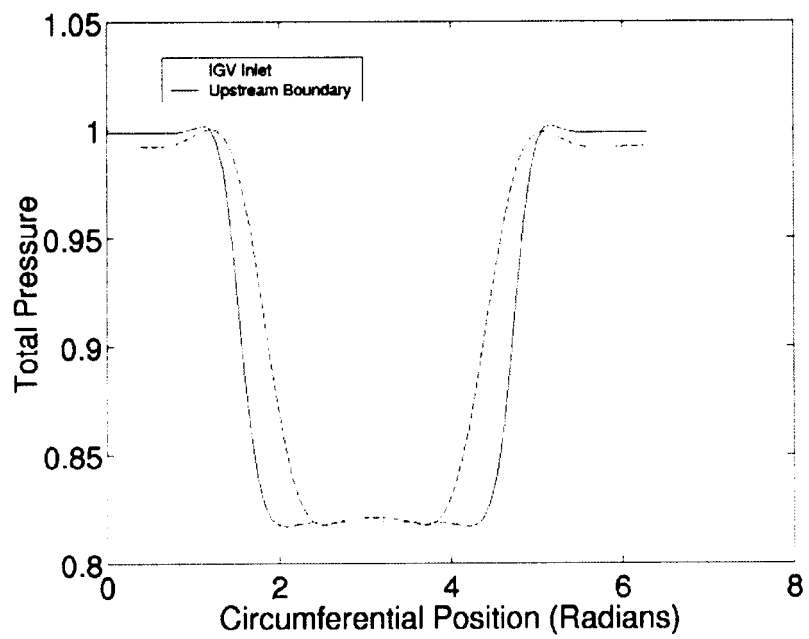
Fig. 3.8 Total Pressure at Mid-span of the IGV Inlet, Showing Reduction of Circumferential Extent of Low Total Pressure Region from Upstream Boundary to IGV Inlet.
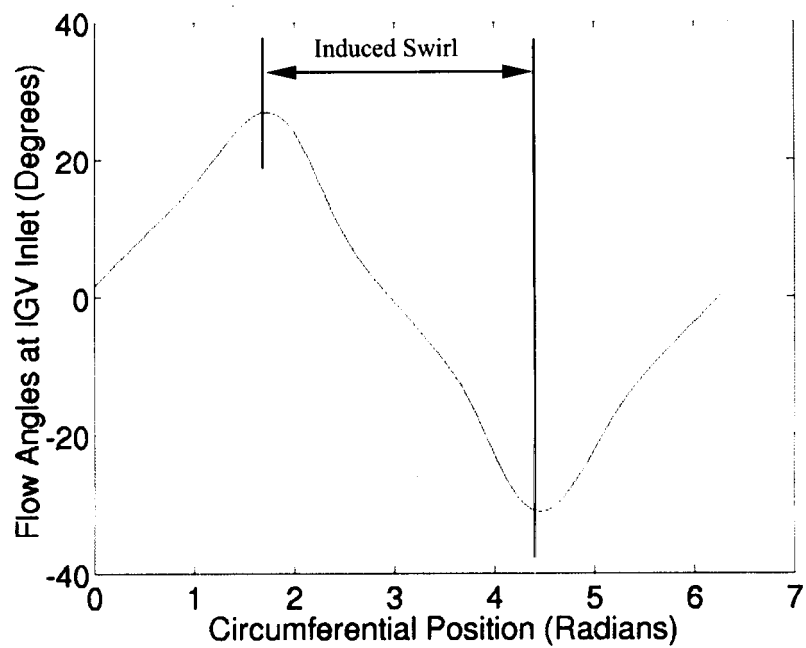

Fig. 3.9 Flow Angles at IGV Inlet, Showing Induced Swirl.

3.4 Distortion Propagation Through Compressor Stages

Having established the occurrence of a static pressure distortion at the IGV inlet, this section examines its propagation through the compressor stages. The manner in which the propagation occurs will lead to an understanding as to why deterioration in total pressure ratio is particularly significant in the last 2 stages as compared to the other stages (Fig. 3.1).

The key features of the propagation of the static pressure distortion are

● Amplification through the first 9 stages

● Strong attenuation within the last 2 stages, resulting in no circumferential variation at the compressor exit. It will be shown that this takes place in a manner, which leads to severe deterioration in total pressure ratio.

These features are illustrated in Fig. 3.10 which shows the mid-span static pressure range at the inlet of each stage and will be further described in Sections 3.4.1 and 3.4.2. Static pressure range is defined as $\dfrac{P_{max} - P_{min}}{\dfrac{1}{2}\rho U^2}$ at the mid-span and is used here as a measure of the severity of distortion.
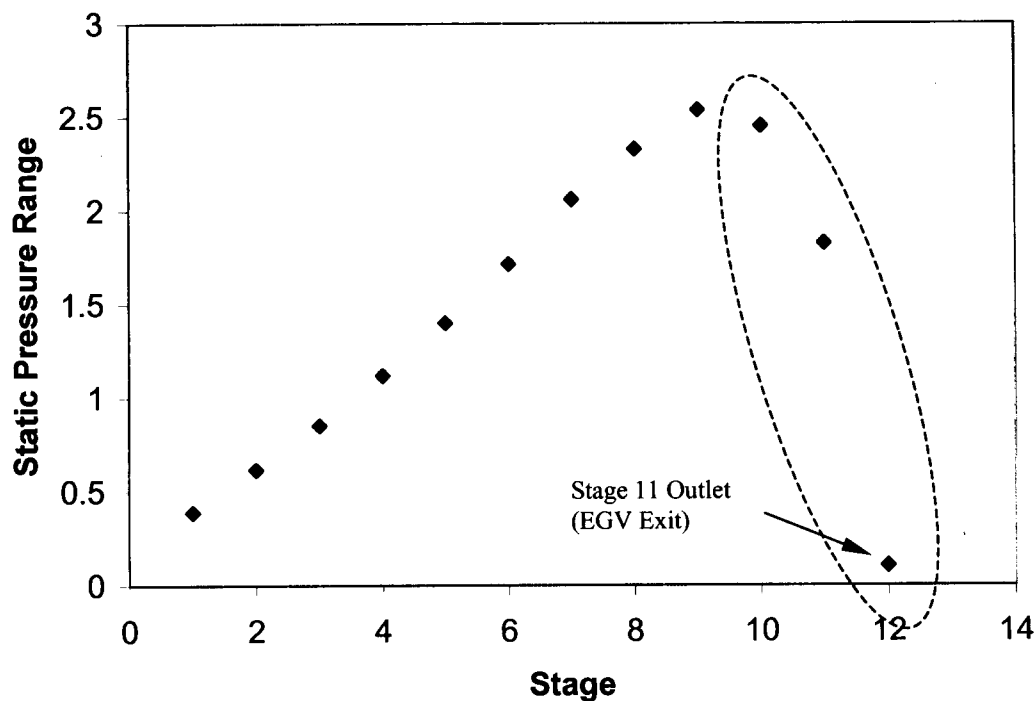
Fig. 3.10 Range of Static Pressure for Each Stage, with the Circled Region Showing Strong Attenuation in Static Pressure Distortion Across the Last 2 Stages

3.4.1 Amplification of Static Pressure Distortion Through First 9 Stages

The amplification effect of the static pressure distortion is observed, from inspection of data at various axial locations as shown in Fig. 3.11, to occur through the first 9 stages.
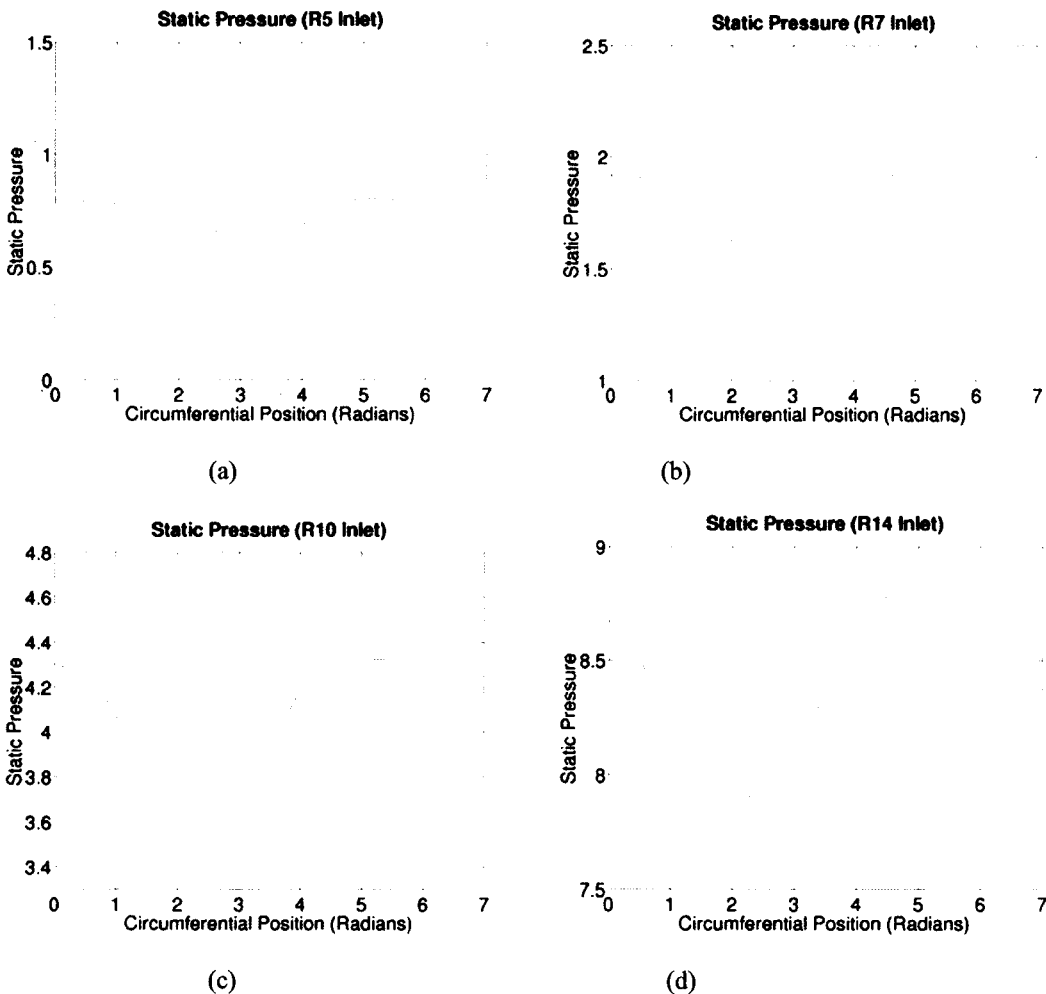
Fig. 3.11 Amplification of Static Pressure Distortion, as Shown by Mid-span Static Pressure at (a)Stage 1 Inlet, (b)Stage 3 Inlet, (c) Stage 5 Outlet and (d)Stage 9 Outlet

3.4.2   Attenuation of Static Pressure Distortion Through Last 2 Stages

The static pressure distortion cannot be amplified throughout the compressor, but must be attenuated at some stage since the condition of uniform static pressure at the compressor exit must be satisfied. The attenuation is achieved in the last 2 stages, most noticeably in the last stage (stage 11), as shown in Fig. 3.12 which shows the pressure distortion at mid-span being abruptly eliminated, resulting in a uniform distribution at the compressor exit (stage 11 outlet).

Closer examination of Fig. 3.12 shows that the elimination of the distortion involves static pressure reduction in certain areas. The total pressure also falls in these areas, as shown in Fig. 3.13 which plots P_t/P_{ref}. Upon examining the mass-averaged total pressure rise across each of the 11 stages as shown in Fig. 3.14, it is found that the mass-averaged total pressure actually falls across stage 11, resulting in the severe deterioration in total pressure ratio over the clean inlet condition, as observed previously in Fig. 3.1. It is uncertain as to how the number of stages over which amplification or attenuation takes place could be determined. Future work in this area is recommended.
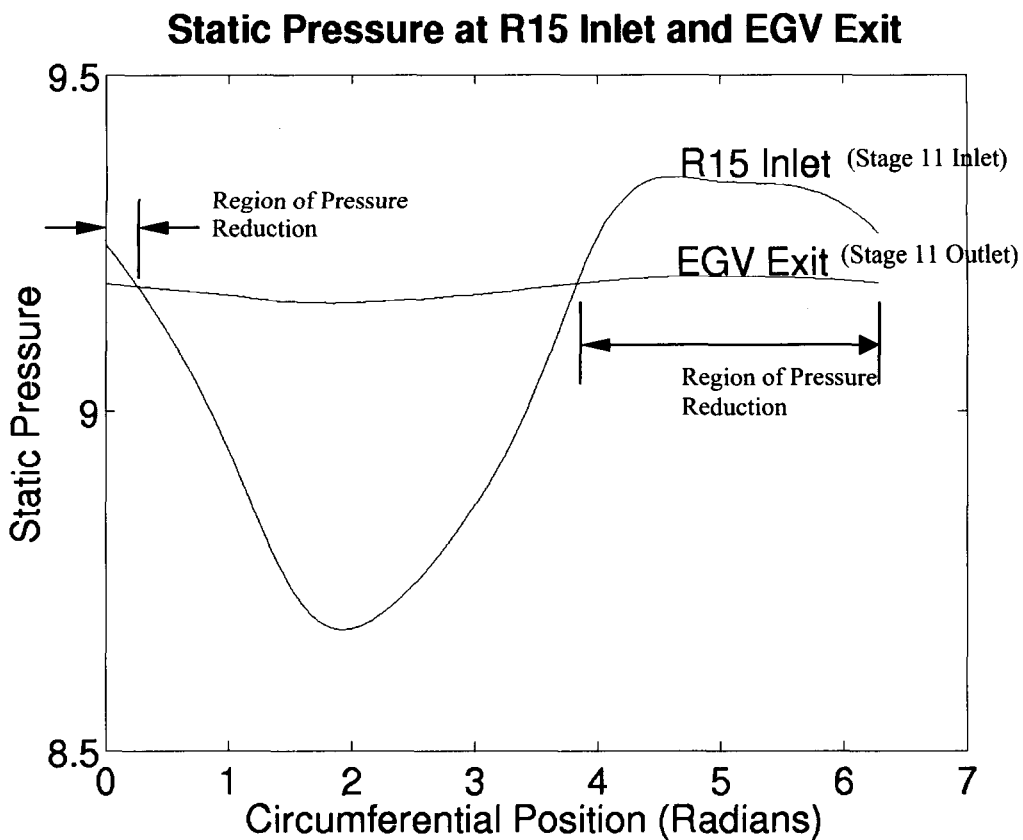
Static Pressure at R15 Inlet and EGV Exit

Fig. 3.12 Elimination of Static Pressure Distortion Across Stage 11, Showing Regions in which Pressure is Reduced
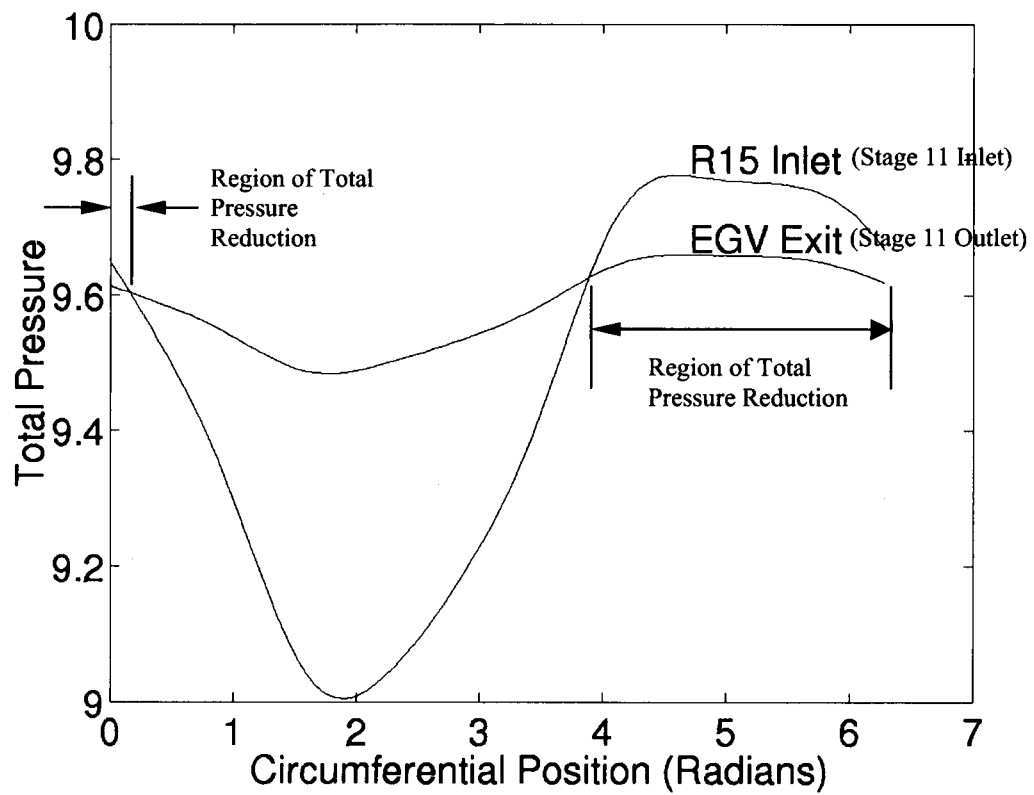
Total Pressure at R15 Inlet and EGV Exit

Fig. 3.13 Total Pressure at R15 Inlet and EGV Exit (Stage 11 Inlet and Outlet Respectively), Showing Regions in which Total Pressure is Reduced
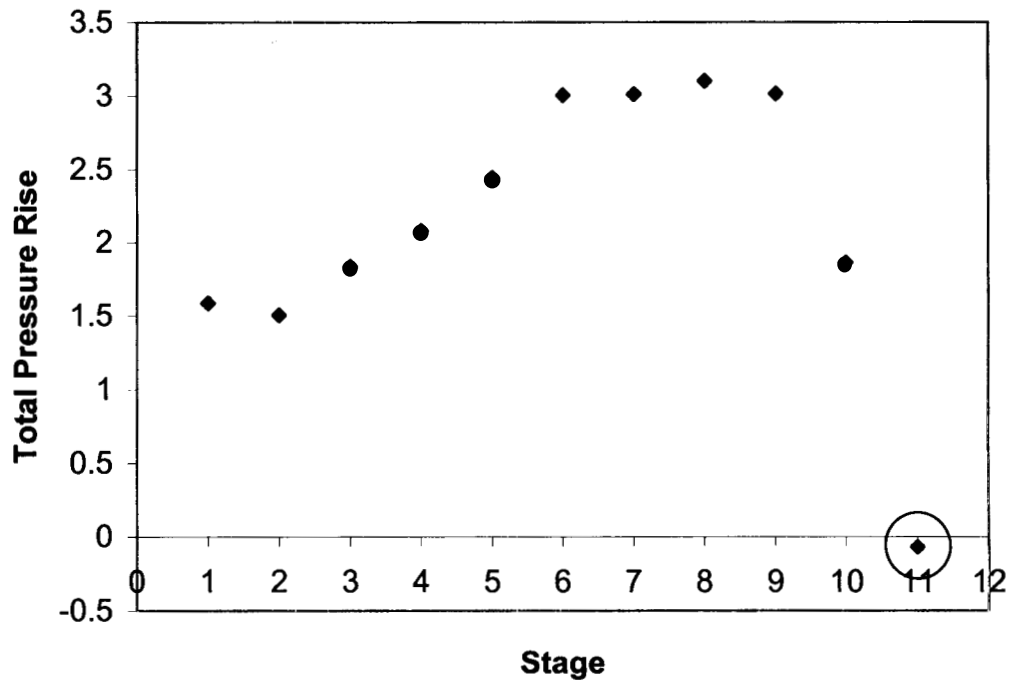
Fig. 3.14 Total Pressure Rise Across Each Stage, Showing that Total Pressure Actually Falls Across Stage 11 (Circled). Total Pressure Rise for a Stage is

Defined as $\dfrac{P_{t,outlet} - P_{t,inlet}}{\dfrac{1}{2}\rho U^2}$

3.5 Summary and recommendations for future work.

The concepts and the procedure developed in Task I and Task III have been used to determine the response of an eleven-stage high-speed compressor to an inlet distortion of 180^0 circumferential extent for contrasting against its performance under uniform inlet flow. Using the computed results at the inlet to and outlet of the compressor, the computed total pressure ratio and efficiency for the clean condition are 14.22 and 76.9% respectively. Similarly, for the distorted case, these are 10.35 and 71.8% respectively, showing a deterioration in efficiency of 5%. For the eleven stage compressor examined here, the deterioration in performance has been found to be particularly severe in the last 2 stages. This suggests that the last two stages could be redesigned to alleviate the observed

deterioration thus making the compressor performance insensitive to circumferential inlet distortion.

Task IV has only addressed the performance of the eleven stage high-speed compressor in response to a circumferential inlet distortion in terms of resulting change in pressure ratio and efficiency. The next step would be the application of such a framework to address the operability issues of compressor due to inlet distortion of various types.